International Journal of Mechanical Sciences 207 (2021) 106630

Contents lists available at ScienceDirect

International Journal of Mechanical Sciences

journal homepage: www.elsevier.com/locate/ijmecsci

Inertial amplification band-gap generation by coupling a levered mass with a locally resonant mass

Arnab Banerjee[a], Sondipon Adhikari[b], Mahmoud I. Hussein[c,d,*]

[a] Department of Civil Engineering, Indian Institute of Technology Delhi, India
[b] College of Engineering, Swansea University, Swansea, UK
[c] Smead Department of Aerospace Engineering Sciences, University of Colorado Boulder, CO, USA
[d] Department of Physics, University of Colorado Boulder, CO, USA

ARTICLE INFO

Keywords:
Elastic metamaterials
Inertial amplification
Local resonance
Band gaps
Elastic waves
Vibration attenuation

ABSTRACT

Inertial amplification has been utilized in phononic media as a mechanism for the generation of large band gaps at low subwavelength frequencies. A unique feature in an inertial-amplification band gap is that it may exhibit two coupled peaks in the imaginary wavenumber portion of its band diagram. This unique double-attenuation band gap has been shown to emerge from a periodic arrangement of a levered mass whose motion is directly connected to that of an independent degree of freedom in the system through the motion of the lever base. Here we demonstrate a double-attenuation band gap emerging specifically from a modal coupling of the levered mass with a conventional local-resonance mass separately attached to the base. This presents a fundamentally distinct mechanical mechanism for the shaping of inertially-amplified band gaps and provides a pathway for realising a combination of strength and breadth in the wave attenuation characteristics. We theoretically present this concept, analytically identify critical conditions for the coupling of the attenuation peaks, and provide a series of parametric sweeps to further highlight the phenomenon and guide design. For example, we find a design with a relatively elevated level of minimum attenuation over practically the entire width of a band gap with a relative size of 130%, and another design with a smaller band gap but a 15-fold increase in the minimum attenuation strength compared to a pure IA chain.

1. Introduction

The generation of frequency band gaps (stop bands) within which waves spatially attenuate is one of the coveted characteristics of periodic structures [1–3]. This concept has attracted research from a variety of disciplines, including vibrations, structural dynamics, acoustics, and materials physics. In an attenuation band, a free or driven wave cannot propagate, and instead experiences exponential attenuation along the direction of propagation. The most common band-gap formation mechanism is based on wave interferences and Bragg scattering. Destructive interferences of transmitted and reflected waves from periodic inclusions, interfaces, and/or boundaries within the medium is the unerlying cause behind the formation of Bragg scattering-based band gaps [4,5]. Band gaps may also emerge due to local resonances; these may be realized in an elastic or acoustic waveguide with intrinsically embedded or attached resonators (usually distributed periodically) [6,7]. The key mechanism for locally resonance band gaps is a coupling—a hybridization—between substructure resonance modes and elastic wave modes in the hosting medium.

Given the practical benefits of band gaps, it is often desirable to find unit-cell configurations that exhibit band gaps that are both as low and wide as possible in the frequency domain; see, for example, Refs. [8–12] for Bragg band gaps and Refs. [13–15] for local-resonance band gaps. Band-gap enlargement by possibly utilizing more than one band-gap mechanism in a combined manner has also been pursued [16,17]. Relatively wide Bragg band gaps may be realized by careful unit-cell topology design and optimization [8–10]; however, the unit cell is fundamentally constrained to be on the order of the wavelength of the interfering waves. This, in turn, implies relatively high-frequency band gaps when the unit cell is small. On the other hand, while local resonances provide an effective path towards realizing low-frequency, subwavelength band gaps with small unit cells (since resonance couplings are independent of wave interferences across periodic features), these tend to be overly narrow and require a relatively heavy resonator to drop significantly in the frequency domain [18]. To address these limitations, the mechanism of inertial amplification has been introduced as an alternative for band-gap generation in structured media [19–21]. Inertial amplification represents a contrast to local resonance in a subtle manner

* Corresponding author at: Smead Department of Aerospace Engineering Sciences, University of Colorado Boulder, CO, USA.
E-mail addresses: abanerjee@iitd.ac.in (A. Banerjee), s.adhikari@swansea.ac.uk (S. Adhikari), mih@colorado.edu (M.I. Hussein).

https://doi.org/10.1016/j.ijmecsci.2021.106630
Received 9 April 2021; Received in revised form 22 June 2021; Accepted 26 June 2021
Available online 2 July 2021

because it involves a mechanical mechanism to provide a magnification of the "effective inertia" of a resonator. This concept has been realized by the introduction of a lever-arm effect whereby the inertia of a resonating mass is magnified to a degree proportional to the arm length. A unique feature that emerges in certain implementations is the existence of a double-peak in the attenuation profile which is represented in the imaginary part of the dispersion diagram [22]. Compared to a single peak—which is realized in an IA chain with only one independent degree of freedom in the unit cell [23]—a double peak provides a frequency range with a significantly higher spatial attenuation strength. These traits bring rise to band gaps that can be both low, wide, and highly attenuating–all while keeping the unit cell size within the subwavelength regime. Upon reduction to its canonical form, inertial amplification is realized by introducing a classical inerter element into a locally resonant mass-in-mass chain [24], as demonstrated by Kulkarni and Manimala [25] and Al Ba'ba'a et al. [26]. Since its introduction in 2007 by Yilmaz et al., the concept of inertial amplification in phononic media has been attracting increasing attention among the phononics community; see, e.g., Refs. [22,27–31].

In previous studies of inertially amplified (IA) phononic materials/structures, the double peak in the attenuation spectrum stem from a direct connection between an IA mass (which exhibits an antiresonance) and an independent degree of freedom associated with another component in the system causing the generation of a second antiresonance (possibly due to a local resonance effect).[1] This enables combined frequency breadth and spatial attenuation strength for the band gap, whereas the location of the IA antiresonance is determined by the level of amplification—which in turn is controlled by levering the acceleration of the IA mass using a rigid, or rigid-like, link. These features create an IA mechanism that either define the backbone configuration of a phononic waveguide [19–21] or serve as an attachment to a standard continuous elastic structure such as a rod [22] or a beam [28]. In the latter cases, the IA modal mass is coupled to a modal degree of freedom associated with the motion of the supporting continuous base. In contrast, in this paper we present a mechanism whereby the generation of the double-peak attenuation band gap is obtained from a modal coupling of an IA mass and a locally resonant mass separately attached to the base waveguide. This intrinsic and coupled mixing of the motion of an IA mass and that of a conventional attached local resonator to open up a wide subwavelength band gap with two coupled peaks in the imaginary wavenumber domain represents a novel concept with significant implications on band-gap design. We present a lumped-parameter model realising this concept, and derive the corresponding complex dispersion relation. An analytical expression is also provided that characterizes the coupling conditions. A parametric analysis is then carried out to identify the sensitivity of the governing parameters on the attenuation properties. Three metrics are proposed for quantifying the performance of this type of band gap. The behavior of these performance metrics with variation in the governing design parameters are then examined to pave the way for realization of optimized configurations. Effective mass and stiffness properties are also calculated to add further insight. Finally, we present at the end of our investigation a direct comparison—on both infinite and finite chains–between the response when the resonator mass is included versus when it is removed.

2. Mathematical modeling of the proposed inertial amplifier chain

Our proposed inertially amplified chain is depicted in Fig. 1(a). Two successive baseline masses M are connected to each other with a baseline spring K and a pair of inertial amplifiers each of mass m_a. Each inertial amplifier mass is levered with rigid links and is restricted to move only along the vertical direction, as illustrated in Fig. 1. These inertial amplifier masses play the key role in inducing inertial amplification, as their accelerations are amplified owing to the lever-arm formed by the connecting mechanism. To introduce a "tuning knob" for the level of inertial amplification, a vertical spring with stiffness k_a, termed the vertical stiffness of the inertial amplifier, is introduced as shown in Fig. 1(b). When the value of k_a is set to zero, maximum inertial amplification is attained. As it is increased, the level of inertial amplification decreases representing an effective loss of rigidity in the connecting link. In the limit of high vertical stiffness, the levered masses transition their behavior to standard local resonance (see analysis in the following section).

2.1. Effective mass formulation for the local-resonance mass attached to the baseline chain

As mentioned above, a spring-mass linear resonator is attached to the base chain. The modal degree of freedom associated with the linear spring-mass resonator may be tuned to couple with that associated with the identical inertially amplified masses and thus creating a band gap with a double-attenuation peak in the imaginary part of the dispersion diagram; this aspect is discussed and analysed in the next sections. First we will examine the dynamic effective mass stemming from this unique configuration. The equation of motion of the resonating mass can be written as

$$\begin{aligned} &m\ddot{w}_x + k(w_x - u_n) = 0 \quad \text{or} \\ &w_x = \frac{1}{1-\left(\frac{\omega^2}{\omega_r^2}\right)}u_n = \frac{1}{1-\left(\frac{\omega^2}{\omega_s^2}\frac{\omega_s^2}{\omega_r^2}\right)}u_n \quad \text{or} \\ &w_x = \frac{1}{1-\frac{\Omega^2}{\eta_r^2}}u_n, \end{aligned} \tag{1}$$

where u_n and w_x denote the displacement of the baseline mass and local resonator mass, respectively, ω is the free wave frequency, $\omega_s^2 = K/M$ is the natural frequency of the base chain mass/spring, $\omega_r^2 = k/m$ is the natural frequency of the local resonator mass/spring, Ω is a non-dimensional frequency ratio defined as $\Omega = \omega/\omega_s$, and η_r is a non-dimensional frequency ratio which can be written as $\eta_r = \omega_r/\omega_s$.

The frequency-dependent effective baseline mass M_e can be computed from the momentum balance as follows:

$$\begin{aligned} &M_e\ddot{u}_n = m\ddot{w}_x + M\ddot{u}_n \quad \text{or} \\ &M_e = M\underbrace{\left(1 + \frac{\theta_r}{1-\left(\frac{\Omega}{\eta_r}\right)^2}\right)}_{\chi_m}, \end{aligned} \tag{2}$$

where $\theta_r = m/M$ is defined as a dimensionless parameter.

2.2. Force on the main mass from the inertial amplifier masses

From the system kinematics, the relationship between the acceleration of the auxiliary masses $\ddot{v}_n$ and the acceleration of the main mass $\ddot{u}_n$ and $\ddot{u}_{n-1}$ can be expressed as

$$\begin{aligned} &v_n = \frac{(u_n - u_{n-1})}{2}\cot\alpha \quad \text{or} \\ &\ddot{v}_n = \frac{(\ddot{u}_n - \ddot{u}_{n-1})}{2}\cot\alpha, \end{aligned} \tag{3}$$

where α is the angle of the rigid-link with the axial axis of the base chain, as shown in Fig. 1. The force on the rigid links can be calculated by

[1] This appears in both IA materials (represented by infinite models) [22] and IA structures (represented by finite models) [20–22].

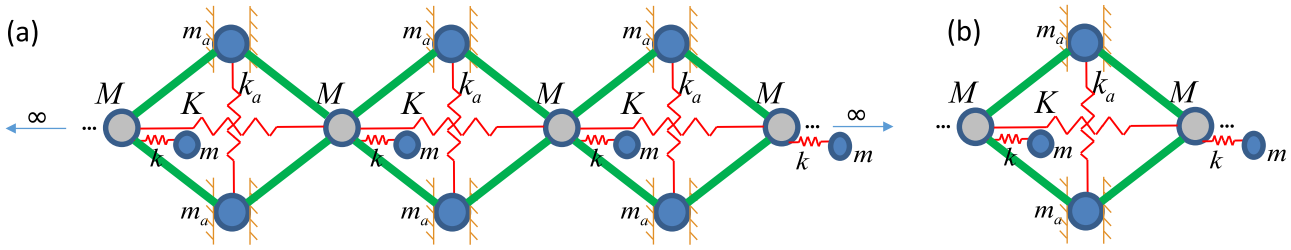

Fig. 1. (a) Proposed IA chain comprising a levered mass and a locally resonant mass. (b) A single representative unit cell.

balancing the forces acting at the mass of each of the inertial amplifiers as

$$2F_n \sin\alpha = m_a \ddot{v}_n + 2k_a v_n \quad \text{or}$$
$$F_n = \frac{(-\omega^2 m_a + 2k_a)(u_n - u_{n-1})}{4\sin\alpha\tan\alpha}. \tag{4}$$

The force component acting from the inertial amplifier pair on the baseline mass in the direction of the wave propagation is

$$\tilde{F}_n = 2F_n\cos\alpha = \underbrace{\frac{(-\omega^2 m_a + 2k_a)}{2\tan^2\alpha}}_{\chi}(u_n - u_{n-1}). \tag{5}$$

2.3. Equation of motion of the overall chain

The governing equation of motion for the nth baseline mass in the chain is as follows:

$$M_e\ddot{u}_n + K(2u_n - u_{n-1} - u_{n+1}) + \tilde{F}_n - \tilde{F}_{n+1} = 0, \quad \text{or}$$
$$(-\omega^2 M_e + 2K_e)u_n - K_e u_{n+1} - K_e u_{n-1} = 0, \tag{6}$$

where M_e and K_e are the dynamic effective baseline mass and stiffness of the overall chain as shown in Fig. 1.[2] The effective stiffness K_e can be expressed as $K + \chi$ where χ is defined as shown in (5). From Bloch's theorem, the displacement of the successive units can be written as:

$$u_{n+1} = u_n e^{i\mu} \quad \text{and} \quad u_{n-1} = u_n e^{-i\mu}, \tag{7}$$

where a is the length of the unit cell, q is the wavenumber, and the dimensionless quantity qa is represented by μ. Substituting (7) into (6), we derive the dispersion relationship as

$$(-\omega^2 M_e + K_e(2 - e^{i\mu} - e^{-i\mu}))u_n = 0 \quad \text{or}$$
$$\frac{\omega^2 M_e}{K_e} = 2(1 - \cos\mu) \quad \text{or}$$
$$\mu = \cos^{-1}\left(1 - \frac{\omega^2 M_e}{2K_e}\right), \tag{8}$$

The effective stiffness K_e, in turn, reads as

$$K_e = K + \frac{(-\omega^2 m_a + 2k_a)}{2\tan^2\alpha} = K + \frac{k_a}{2\tan^2\alpha}\left(2 - \frac{\Omega^2}{\eta_a^2}\right)$$
$$= K\left(1 + \beta\left(2\eta_a^2 - \Omega^2\right)\right). \tag{9}$$

where

- $\beta = [\theta/(2\tan^2\alpha)] = [m_a/(2M\tan^2\alpha)]$ is the inertial amplification factor; it is a parameter that represents the ratio of the inertial amplifier mass m_a to the baseline mass M considering the influence of the angle of the inertial amplifier α. The parameter $\theta = m_a/M$ is the ratio of the inertial amplifier mass to the baseline mass.
- $\eta_a = \omega_a/\omega_s$ is the ratio of the inertial amplifier/vertical spring natural frequency $\omega_a = \sqrt{k_a/m_a}$ to the base chain mass/spring natural frequency $\omega_s = \sqrt{K/M}$.
- $\theta_r = m/M$ is the ratio of the resonator mass to the base chain mass.
- $\eta_r = \omega_r/\omega_s$ is the local resonator frequency ratio, defined as the ratio of the local resonance mass/spring natural frequency $\omega_r = \sqrt{k/m}$ to the base chain mass/spring natural frequency $\omega_s = \sqrt{K/M}$.

2.4. Band gaps

A propagation band may be identified from the range of $\cos\mu$ of (8); this is because a real μ corresponds to a propagating wave:

$$-1 \le \cos\mu \le 1 \quad \text{or}$$
$$0 \le \frac{\omega^2 M_e}{K_e} \le 4 \quad \text{or}$$
$$0 \le \frac{\Omega^2\left(1 + \frac{\theta_r\eta_r^2}{\eta_r^2 - \Omega^2}\right)}{1 + \beta(2\eta_a^2 - \Omega^2)} \le 4 \tag{10}$$

It can be seen that (10) depends only on four non-dimensional parameters: β, η_a, η_r and θ_r. For $\eta_a = 0$, the inequality of (10) can be further simplified as follows:

Propagating waves:

$$\begin{cases} 0 \le \Omega \le \Omega_{c1} \,||\, \Omega_{c2} \le \Omega \le \eta_r\sqrt{1+\theta_r} & \text{if } \eta_r^2 > \frac{1}{\beta(1+\theta_r)} \\ \eta_r\sqrt{1+\theta_r} \le \Omega \le \sqrt{\frac{1}{2}\left(\epsilon_1 + \sqrt{\epsilon_2}\right)} & \text{if } 0 < \eta_r^2 < \frac{1}{\beta(1+\theta_r)} \end{cases} \tag{11}$$

where $\Omega_{c1} = \sqrt{\frac{1}{2}(\epsilon_1 - \sqrt{\epsilon_2})}$, $\Omega_{c2} = \sqrt{\frac{1}{2}(\epsilon_1 - \sqrt{\epsilon_2})}$, $\epsilon_1 = 4 + \eta_r^2(1 + 4\beta + \theta_r)/1 + 4\beta$, and $\epsilon_2 = 16 - 8\eta_r^2(1 + 4\beta - \theta_r) + \eta_r^4(1 + 4\beta + \theta_r)^2/(1 + 4\beta)^2$. Equation (11) allows us to indirectly predict the locations of the band-gap edges as a function of the model design parameters.

2.5. Effective medium properties

Eqs. (2) and (9) define the frequency-dependent dynamic effective mass and stiffness needed to obtain identical dispersive behavior. The effective mass ratio $\bar{M}$ is the ratio of the effective mass M_e to the baseline mass M, and the effective stiffness ratio $\bar{K}$ is the ratio of the effective stiffness K_e to the baseline stiffness K. These are expressed, respectively, as follows:

$$\bar{M} = \frac{M_e}{M} = \left(1 + \frac{\theta_r}{1 - \left(\frac{\Omega}{\eta_r}\right)^2}\right) \quad \text{or}$$
$$\bar{K} = \frac{K_e}{K} = \left(1 + \beta\left(2\eta_a^2 - \Omega^2\right)\right). \tag{12}$$

In principle, a one-to-one mapping can be realized between the complex dispersion relation and these frequency-dependent effective properties. These quantities will be used in the upcoming subsection in the analysis of the attenuation mechanisms.

[2] For brevity, these quantities will hereafter be denoted as the effective mass and effective stiffness.

2.6. Formation mechanism of double-peak attenuation

Two attenuation peaks are noticed when the effective stiffness is equal to zero, i.e., $\bar{K} = 0$, and the effective mass tends to infinite, i.e., $M_e \to \infty$. From Eq. (12), it can be seen that the stiffness peak Ω_s occurs at $\Omega_s = \sqrt{1/\beta}$ while $\eta_a = 0$ and the mass peak occurs at $\Omega_m = \eta_r$. Additionally, the above condition occurs while a transition of the band-gap character occurs at $\beta\eta_r^2(1+\theta_r) = 1$.

2.7. Analysis of a finite IA chain

In conjunction to Bloch wave propagation analysis of infinite models, it is useful to also examine the response of corresponding finite models. This provides insights into how the wave attenuation characteristics displayed in the imaginary wave number of the dispersion diagrams manifest in a truncated finite system subject to some form of excitation. Implementing the "backward substitution based" method [15] and "momentum balance" technique [32] for a full finite chain, the transmittance and effective mass can be computed by the following approach. The displacement amplitude of the last unit cell in the finite chain is written as:

$$u_{n-1} = \underbrace{\frac{-\omega^2 M_e + K_e}{K_e}}_{B} u_n, \tag{13}$$

whereas, the displacement amplitude of the jth unit cell is expressed as:

$$u_{j-1} = \underbrace{\frac{-\omega^2 M_e + 2K_e}{K_e}}_{A} u_j - u_{j+1}. \tag{14}$$

Solving (14) for the $(n-1)$th cell and proceeding backwards to the second unit cell, we obtain the amplitude of displacement u_1 in terms of u_n. Thus, the transmittance can be easily expressed as $\tau = \log_{10}(u_1/u_n)$. The effective mass, on the other hard, can be computed as:

$$M_e^{\text{fin}} u_n = \sum_{j=2}^{n} M_e u_j \to \bar{M}_e^{\text{fin}} = \frac{M_e^{\text{fin}}}{nM_e} = \frac{1}{n}\sum_{j=2}^{n}\frac{u_j}{u_n}. \tag{15}$$

3. Results and discussion

In this section, we evaluate the dispersion relations derived and present their behavior as a function of the model parameters with a focus on the influence on the attenuation profile in the imaginary part of the band structure diagram.

3.1. Variation of the non-dimensional design parameter β

We start by examining the variation of the inertial amplification factor β, which as described earlier is a function of the ratio θ of inertial amplifier mass m_a to baseline mass M and the rigid-link angle α. This parameter provides a direct representation of the level of effective inertial amplification of the levered mass—which in the static state is m_a—due to variation of the lever angle α. The effect of varying β on the dispersion and attenuation strength generates a multi-dimensional relationship that is plotted in Fig. 2. It is observed that the value of β drastically increases with decreasing angle α and linearly increases with the mass ratio. For example, for $\theta = 0.25$, an angle of $\alpha = 20°$ matches roughly with $\beta = 1$. On the other hand, when α is lowered to only 12° or less, the inertial amplification factor jumps to 3 and higher. The factor $2\tan^2\alpha$ in the denominator in the definition of β (see Section 2.3) determines the level of inertial amplification beyond the static value of m_a. Next, we consider several parametric scenarios exploring limiting cases for the inertially amplified chain.

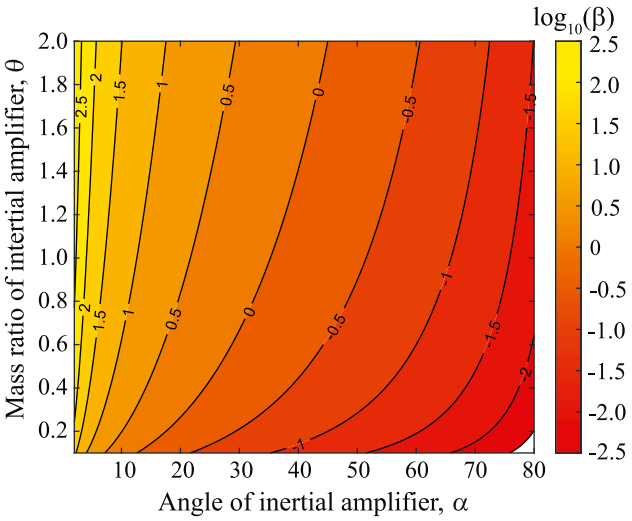

Fig. 2. Variation of the non-dimensional parameter β as a function of the ratio of the inertial amplifier mass to the baseline mass θ and the lever angle α.

3.2. Case 1: No local resonator attached to baseline mass

First, we consider a case with only the inertial amplifier and no local resonator attached to the baseline mass; this configuration has been examined in Ref. [19]. This case is obtained by setting $\theta_r = 0$. Therefore, (10) can be simplified further to

$$0 \le \Omega \le 2\sqrt{\frac{1+2\beta\eta_a^2}{1+4\beta}}. \tag{16}$$

Thus, the attenuation band exists while $\Omega > 2\sqrt{(1+2\beta\eta_a^2)/(1+4\beta)}$ whereas the upper limit of the transmission band is restricted to $\Omega < 2$. The shifting of the attenuation band towards lower frequencies is represented by

$$\varrho = \left(1 - \sqrt{\frac{1+2\beta\eta_a^2}{4\beta+1}}\right) \times 100\%. \tag{17}$$

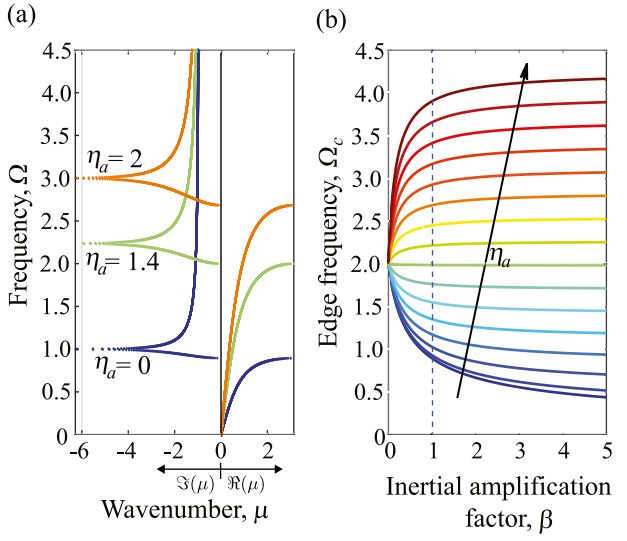

Fig. 3. (Left) Dispersion diagram for $\beta = 1$ and three different values of η_a: 0, $\sqrt{2}$ and 2. (Right) Variation of the band-gap edge frequency Ω_c in terms of β for different values of η_a.

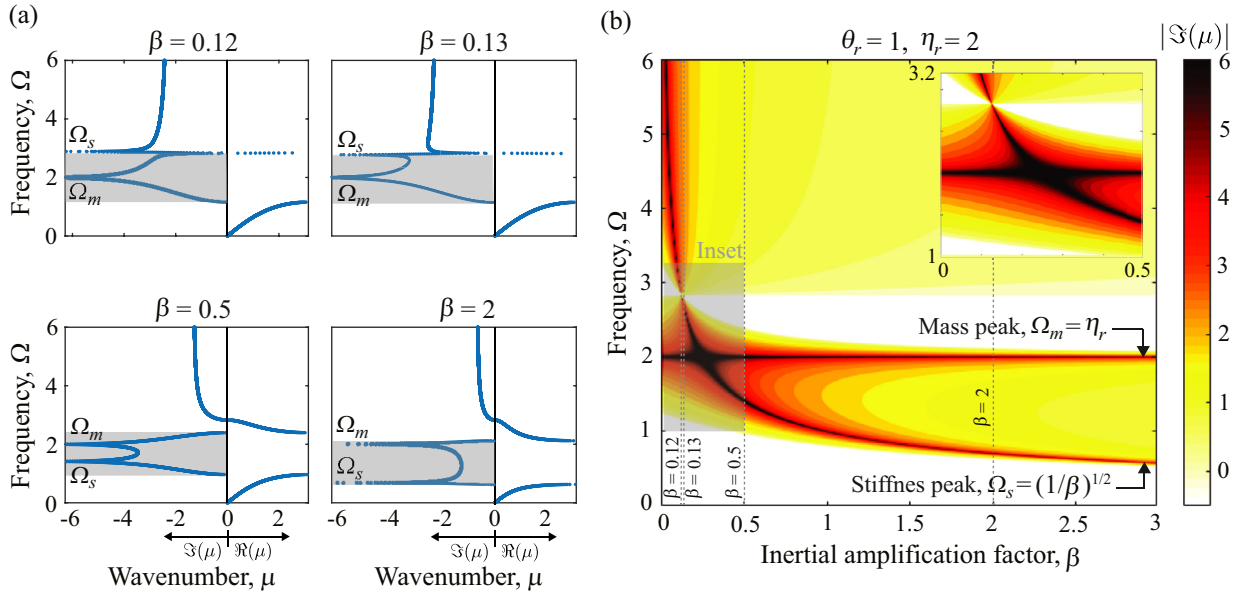

Fig. 4. Effect of the non-dimensional design parameter β on the complex band structure. (a) Dispersion diagrams for four different values of β. (b) Attenuation profile (represented by the normalized imaginary wave number) as a function of frequency Ω and β. For $\beta = 0.12$, the attenuation profile exhibits two uncoupled peaks, the lower one corresponding to a standard local resonance and the higher one representing an IA antiresonance. For $\beta = 0.12$, transition has occurred to an attenuation profile with two coupled peaks. The distance in the frequency domain between the two coupled attenuation peaks is observed to grow with further increase in β. All results are for a vertical stiffness $k_a = 0$, i.e., $\eta_a = 0$.

Here we conclude that the inertial amplifier mass, in the absence of the discrete local resonator, creates only a single attenuation peak in the imaginary wavenumber part of the disperison diagram. While this configuration provides a semi-infinite attenuation profile above the IA antiresonance, the strength of this leveled attenuation (i.e., the maximum value of the imaginary wave number as the frequency goes to infinite) is relatively weak.

Edge frequencies and dispersion relationship. The transmission band is extended from 0 to the edge frequency $\Omega_c = 2\sqrt{(1+2\beta\eta_a^2)/(1+4\beta)}$.

The edge frequency is highly sensitive to two key non-dimensional parameters of the system, namely, the effective mass β and the frequency ratio η_a. The variation of the edge frequency in terms of β and η_a is illustrated in Fig. 3(b). In Fig. 3(a), the concise dispersion diagram for the system having an inertial amplifier mass ratio of $\beta = 1$ and frequency ratio $\eta_a = 0, \sqrt{2}$ and 2 are plotted. It is noticed that a rise in η_a increases the width of the low-frequency propagation band. The edge frequency Ω_c decreases with increasing β when $\eta_a < \sqrt{2}$ and vice-versa.

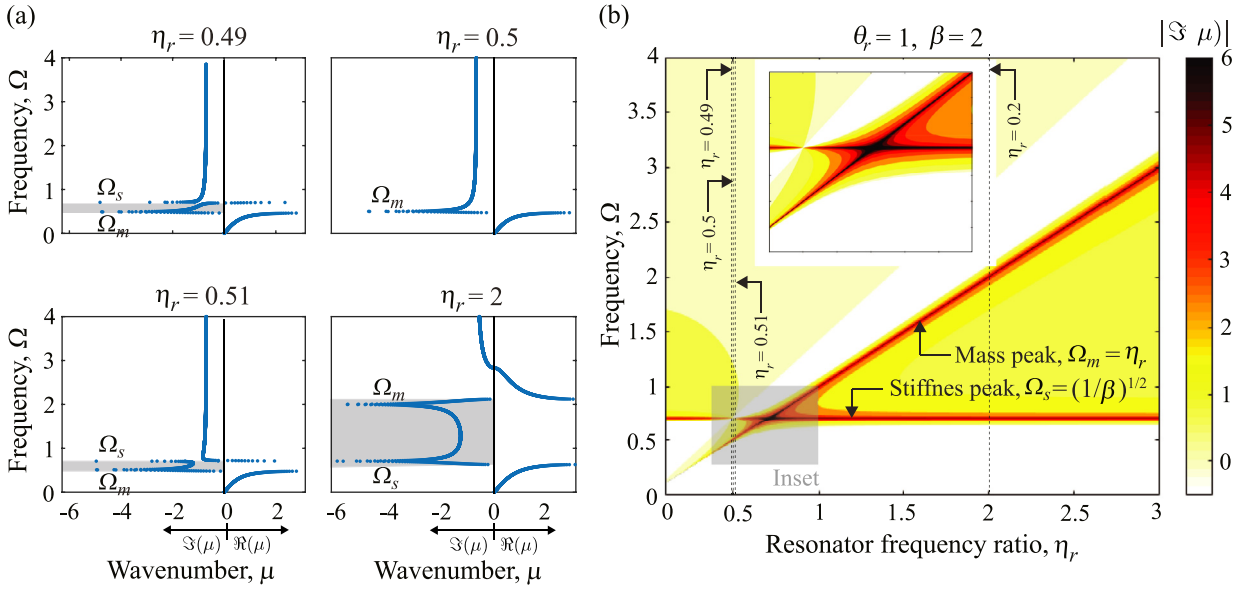

Fig. 5. Effect of the natural frequency ratio η_r on the complex band structure. (a) Dispersion diagrams for four different values of η_r. (b) Attenuation profile (represented by the normalized imaginary wave number) as a function of frequency Ω and η_r. For $\eta_r = 0.49$ the attenuation profile exhibits two uncoupled peaks, the lower one corresponding to a standard local resonance and the upper one representing an IA antiresonance. For $\eta_r = 0.5$, transition has occurred to an attenuation profile with two coupled peaks. The distance in the frequency domain between the two coupled attenuation peaks is observed to grow with further increase in η_r. All results are for a vertical stiffness $k_a = 0$, i.e., $\eta_a = 0$.

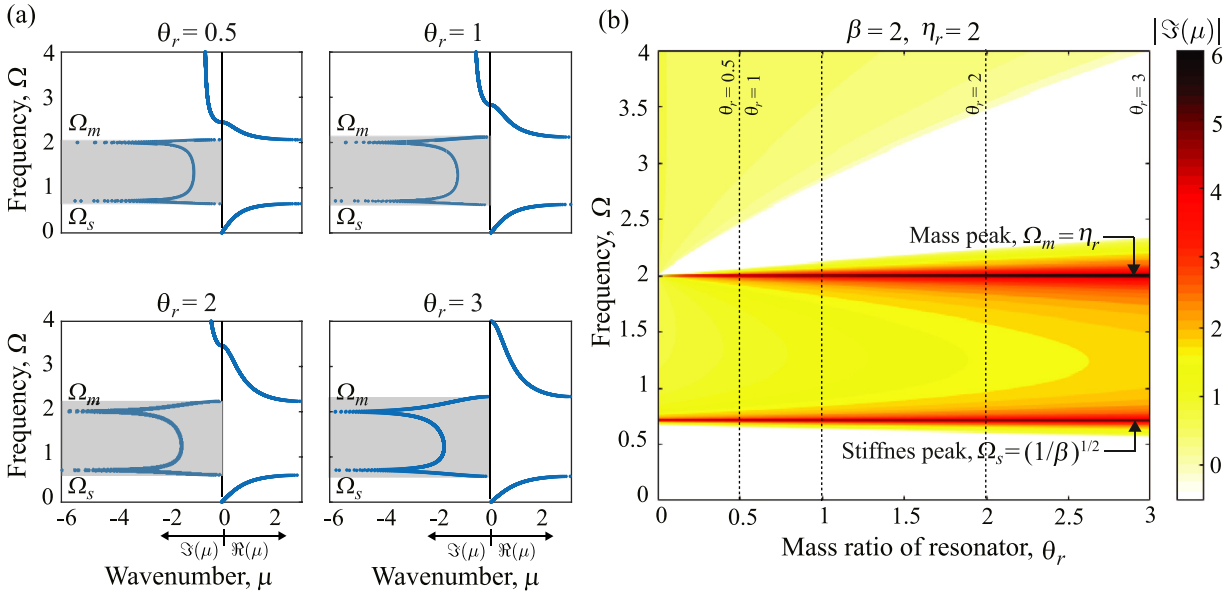

Fig. 6. Effect of the mass ratio θ_r on the complex band structure. (a) Dispersion diagrams for four different values of θ_r. (b) Attenuation profile (represented by the normalized imaginary wave number) as a function of frequency Ω and θ_r. For all values of θ_r considered, the attenuation profile exhibits two coupled peaks. The distance in the frequency domain between the two coupled attenuation peaks is observed to stay nearly constant with further increase in θ_r All results are for a vertical stiffness $k_a = 0$, i.e., $\eta_a = 0$.

3.3. Case 2: Flexible inertial amplifier with a local resonator attached to the baseline mass

Now, a conventional local resonant mass m is attached to the baseline mass M of the chain; we will occasionally refer to this as the "tuning" mass. First, the coefficient of the vertical spring supporting the inertial amplifier—which in practice may be viewed as a representation of the actual stiffness of the joints—is assumed to be $k_a = 0$, which means the frequency ratio of the inertial amplifier is also 0.

3.3.1. Dispersion relations

The complex dispersion diagram including both propagation and attenuation bands (with the strength of the latter indicated by the absolute value in the imaginary wavenumber domain) is computed from (8). The effects of the inertial amplification factor β, the resonator natural frequency ratio η_r, and the resonator mass ratio θ_r on the overall dispersion curves, specifically the attenuation profile, are examined closely in this section.

Figs. 4–6 illustrate the impact on the attenuation profile with varying β, η_r and θ_r, respectively. From Fig. 4, the following observations are noted:

- With increase in inertial amplifier mass ratio β, the IA band gap widens and its central frequency drops to lower values.
- The two attenuation peaks, namely mass peak Ω_m and stiffness peak Ω_s are located where the effective mass and effective stiffness of the medium turns to infinite and zero respectively. Only the stiffness peak shifts to the low frequency side and the mass peak remains constant while β is increased.
- Below a cut off value in β, defined as $\beta^* = 1/[\eta_r^2(1+\theta_r)]$, the double-peak IA attenuation phenomenon cannot be observed. In particular, for $\beta = 0.12$, we notice that the IA antiresonance peak is not coupled with the attenuation peak associated with the local resonance of the tuning mass at $\eta_r = 2.0$. However, for higher values of β these two attenuation peaks couple and generate a relatively large IA band gap with these two peaks appearing inside the band gap.
- A "four-legged" focal point is identified in the β contour diagram indicating a region of maximum attenuation strength. This point is located where $\Omega_s = \Omega_m$.

As for Fig. 5, it illustrates the following:

- The IA band gap width increases with the resonator natural frequency ratio η_r beyond a transitional value of $\eta_r = 0.5$; below this value the chain behaves mostly like a conventional locally resonant chain.
- The location of the mass peak varies with the natural frequency ratio of resonator; however, the stiffness peak remains constant.
- At $\eta_r = 0.5$, the transition point, the attenuation due to the stiffness peak vanishes and a single attenuation peak (mass peak) in the dispersion diagram is noticed.
- At that transitional value, the resonance due to the tuning mass and the inertial amplifier mass matches and a cross-over occurs.

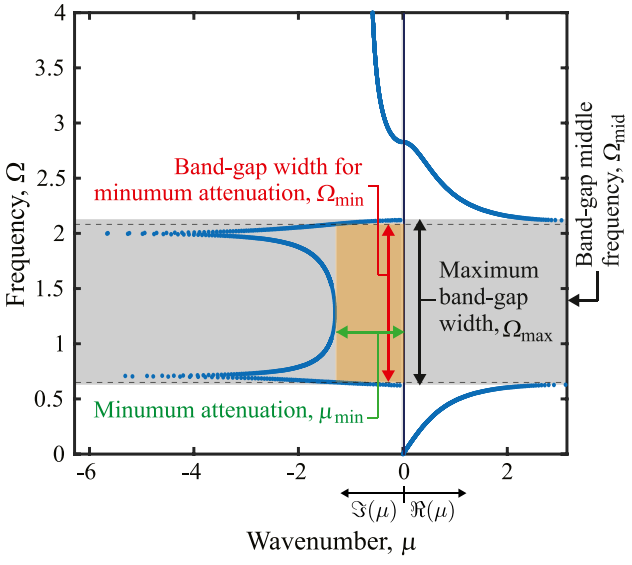

Fig. 7. Illustration of three metrics for the quantification of the relative band-gap size, minimum attenuation level, and relative band gap size corresponding to the minimum attenuation level.

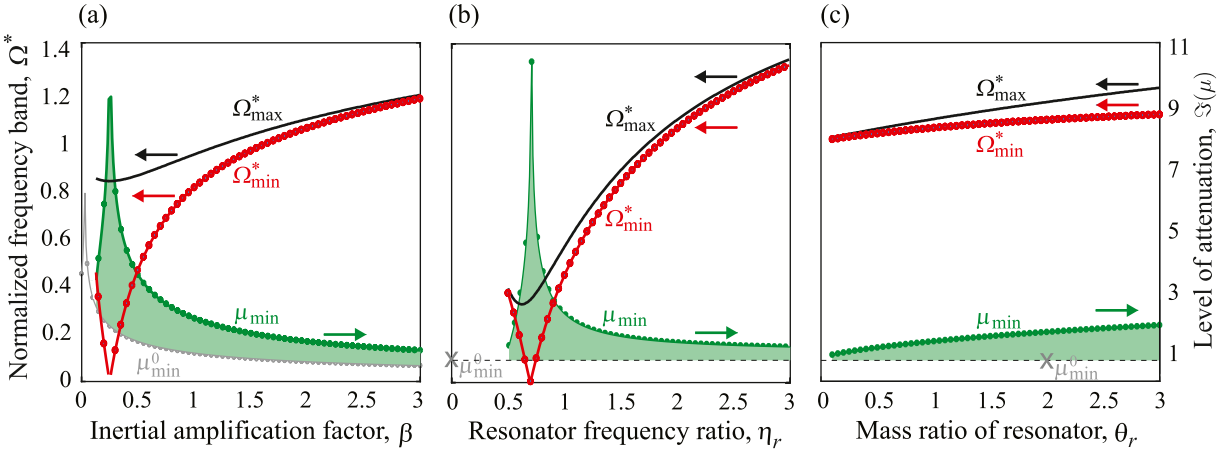

Fig. 8. Variation of the band-gap and attenuation metrics with respect to (a) β, (b) η_r, and (c) θ_r while keeping $\eta_a = 0$.

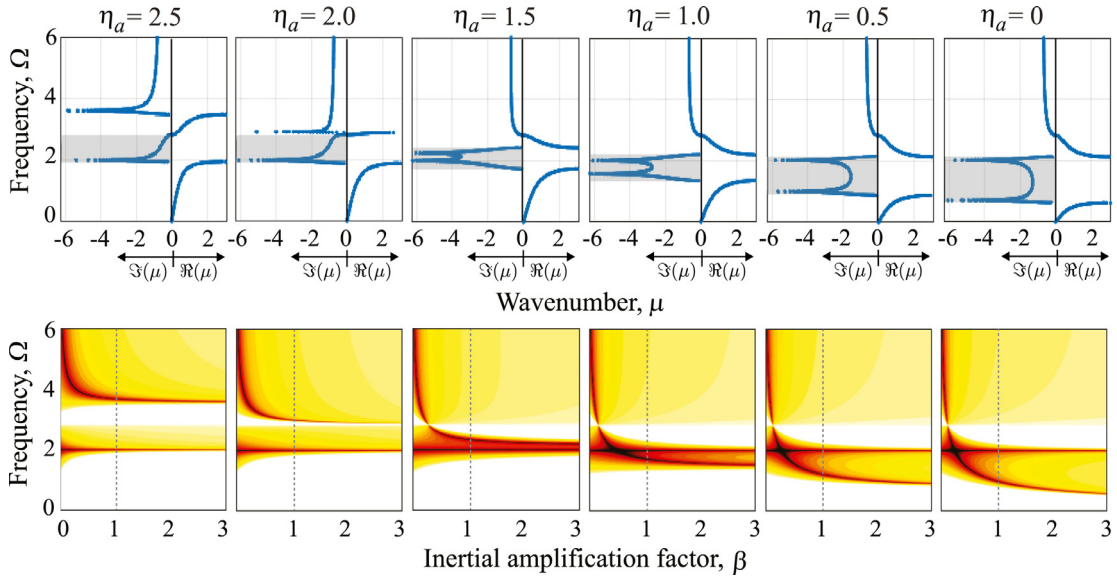

Fig. 9. Band-gap attenuation characteristics as a function of vertical stiffness for the range $\eta_a = 2.5$ to $\eta_a = 0$ (left to right) with an interval of $\Delta\eta_a = 0.5$.

Unlike the previous two cases, the IA band gap and the frequency of the two peaks remain practically constant when the tuning mass ratio θ_r is varied; however, the level of attenuation increases with increasing θ_r, as shown in Fig. 6. The tuning mass may be made to have a more influential effect by changing other parameters in the system as shown below.

3.3.2. *Metrics for band-gap size and attenuation performance*

To quantify the properties of an IA band gap with double attenuation peaks, three metrics are proposed as shown in Fig. 7. The metric $\mu_{\min}$ denotes the minimum level of attenuation achieved within the IA band gap within the frequency range $\Omega_{\min}$ as illustrated in the figure. As for the metric $\Omega_{\max}$, this represents the conventional band-gap width. In both frequency metrics, the bandwidth is normalized with respect to its central frequency value, ω_{mid}. Upon normalization, $\Omega_{\min}$ and $\Omega_{\max}$ are denoted $\Omega^*_{\min}$ and $\Omega^*_{\max}$, respectively. The variation of the metrics as a function of each of β, η_r, and θ_r is plotted in Fig. 8. Fig. 8(a) and (b) illustrate that an IA band gap exists after certain cut-off values of β and η_r, respectively. With increasing β and η_r, beyond certain values, a wider IA band gap is possible at the cost of low level of attenuation $\mu_{\min}$. In contrast, all metrics monotonically increase with θ_r. We observe in Fig. 8(b) that compared to when $m = 0$, a design with a relatively elevated level of minimum attenuation over practically the entire width of the band gap is possible for a band gap with a relative width of 130%. In contrast, a design is possible with a 15-fold increase in $\mu_{\min}$ but with a relatively smaller band-gap size. These results show a trade-off between large band-gap size and minimum attenuation strength. The regions shaded in green in Fig. 8 represent the net "gain" in minimum attenuation strength due to the addition of the locally resonant mass and the consequent generation of the coupled double-peak band gap.

The addition of a locally resonant mass, on the other hand, increases the total weight of the unit cell; this represents a design challenge when there is a constraint on the total weight. Future investigations may explore optimization studies with the additional constraint of keeping the total mass within the unit cell fixed.

3.4. *Inertial amplification with vertical spring with varying stiffness*

To determine the effect of the vertical spring stiffness k_a on the IA band gap and attenuation profile, the inertial amplifier natural frequency ratio η_a is varied; this is shown in the form of the complex dispersion diagram in the top panel of Fig. 9. A contour plot of the attenuation level as a function of the inertial amplification factor β for the different η_a values is plotted in the lower panel of Fig. 9. This figure depicts that as k_a increases, i.e., η_a no longer remains 0, the IA band gap shifts towards

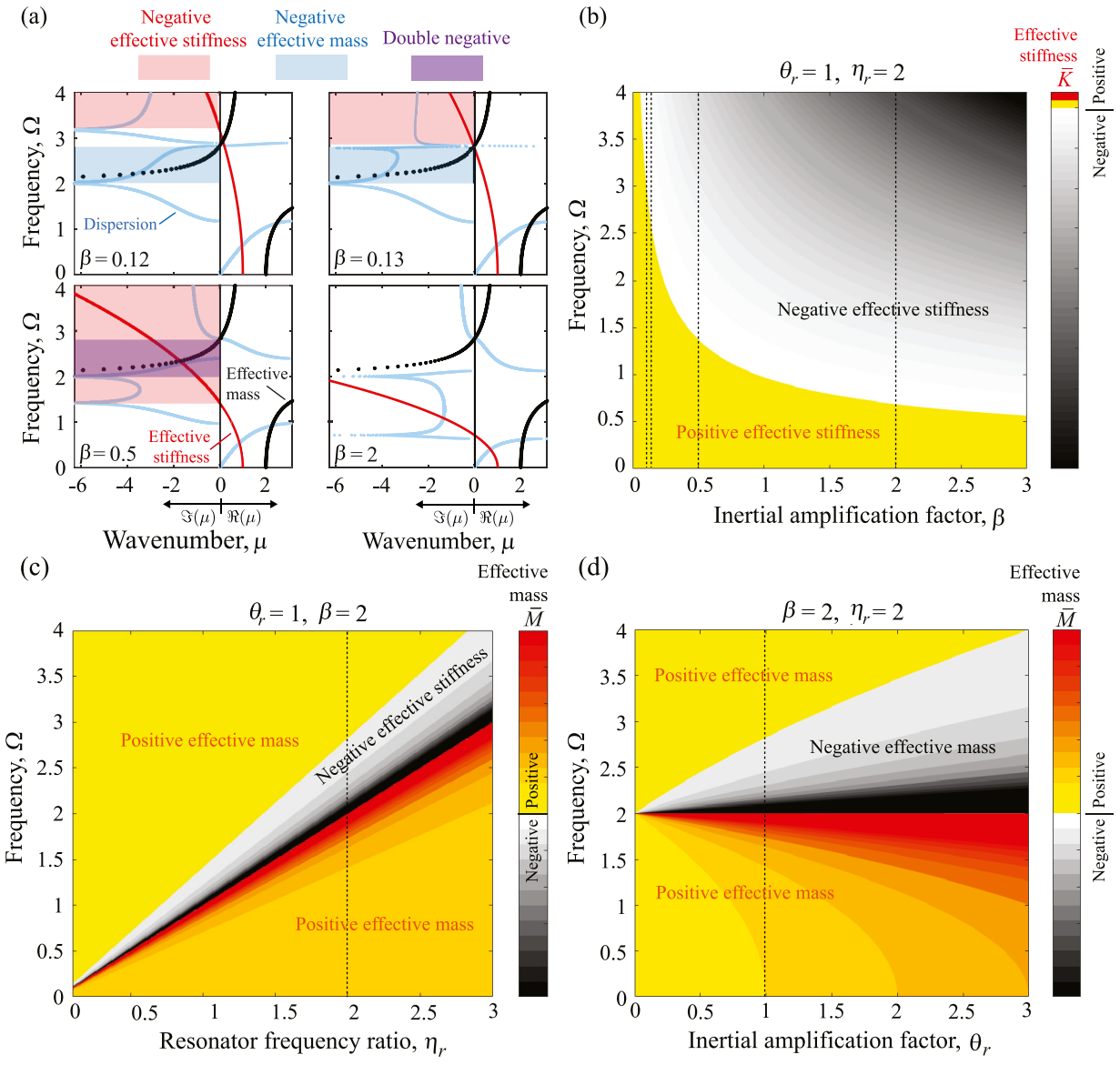

Fig. 10. Dynamic effective properties superimposed on the complex dispersion and corresponding contour plots.

higher frequencies. And, critically, when $\eta_a > \eta_{r1}$, the IA band-gap character is lost and the chain behaves mostly like a conventional locally resonance chain. Therefore, a lower value of k_a is desirable to realize a wider and lower-frequency IA band. This underlies the importance of having a quality lever, with maximum lever rigidity, minimal joint stiffness, etc., when realising this system in practice.

3.5. *Effective properties of the overall elastic waveguide*

Finally, we show that for our proposed inertial amplifier chain, the frequency-dependent dynamic effective mass and effective stiffness exhibit a rich set of properties that vary qualitatively with the key design parameters β, η_r, and θ_r. Specifically, negative effective mass, negative effective stiffness, and dual negative mass and stiffness behavior are realized as indicated in Fig. 10. The following observations are made:

- The dynamic effective stiffness becomes negative over a broad region in the top-right corner of the $\Omega - \beta$ spectrum, in contrast to a narrow region in the $\Omega - \theta_r$ and $\Omega - \eta_r$ spectra.
- The dynamic effective stiffness becomes negative in a narrow region in the bottom-left corner of the $\Omega - \beta$ spectrum, in contrast to broad top-left and bottom-right regions in the $\Omega - \theta_r$ and $\Omega - \eta_r$ spectra.
- Attenuation bands generate in two scenarios:
  1. When either of the dynamic effective medium properties, mass or stiffness, turns negative, or
  2. the inertial force of the effective medium becomes four times higher than the dynamic effective stiffness
- The local resonance attenuation peak corresponds to the dynamic effective mass tending to infinity (denoted as mass peak); and the IA attenuation peak corresponds to the dynamic effective stiffness tending to zero (denoted as stiffness peak).
- When these two attenuation peaks fall between the two edge frequencies, i.e., Ω_{c1} and Ω_{c2}, coupled double-peak attenuation occurs.
- For the set of parameters for which the mass peak and stiffness peak coincide, a significantly high level of attenuation is attained.
- A double negative region emerges where the dynamic effective mass and stiffness are simultaneously negative [33,34]. Observation of a double negative band in a similar chain mode was reported in

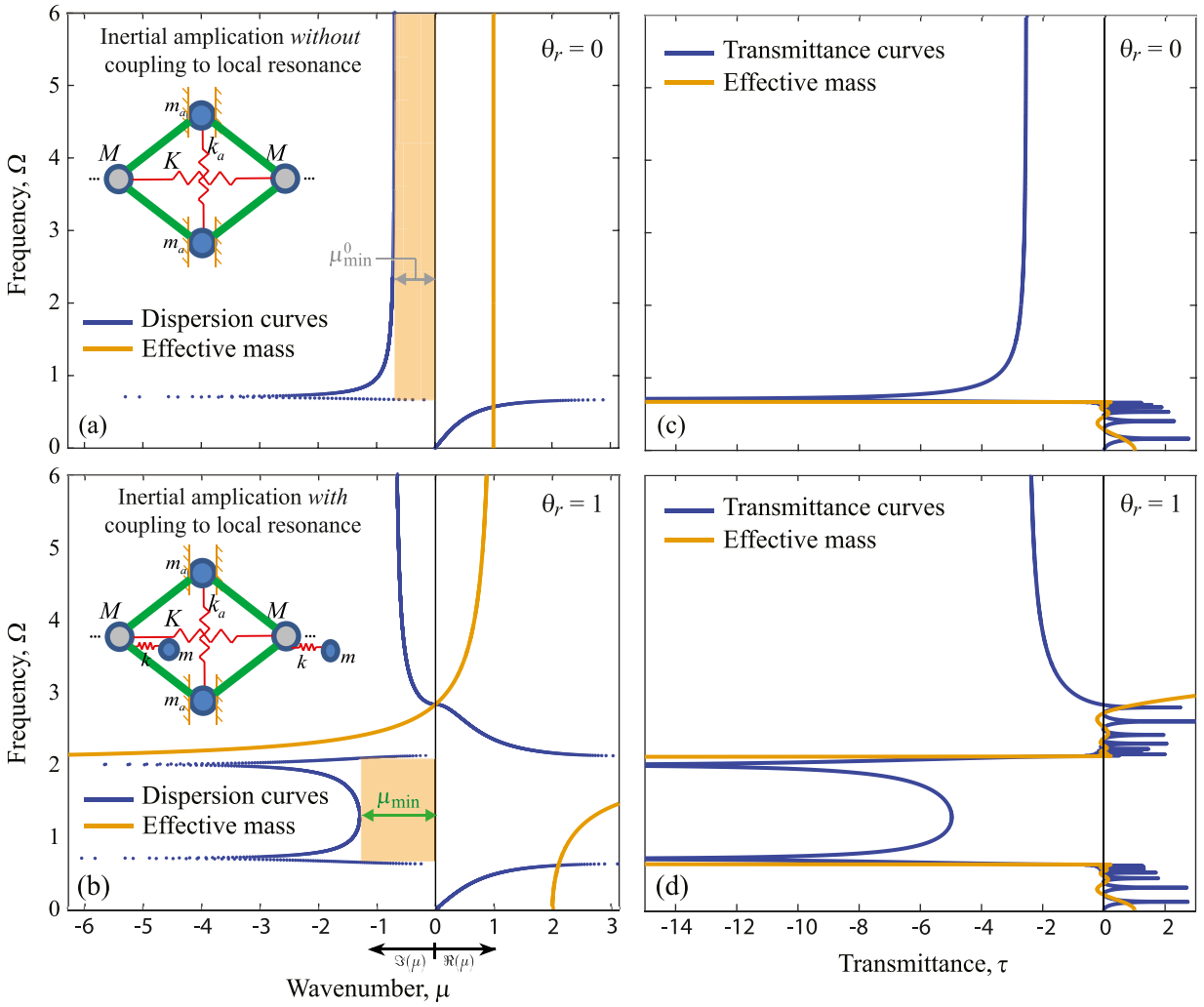

Fig. 11. Dispersion curves (blue; in wavenumber μ) and effective mass (orange; units omitted) for IA chain (a) without added local resonator, i.e. $\theta_r = 0$, and (b) with added local resonator having a mass ratio $\theta_r = 1$. Transmittance curves (blue; in transmittance τ) and effective mass (orange; units omitted) for a corresponding finite chain comprising ten units cells (c) without added local resonator, i.e., $\theta_r = 0$, and (d) with added local resonator having mass ratio $\theta_r = 1$. (For interpretation of the references to color in this figure legend, the reader is referred to the web version of this article.)

Ref. [35], although no reference was made on the possibility of coupled peaks in the attenuation spectrum.

3.6. Transmittance and effective mass in truncated finite chain

The results illustrated in Fig. 11 provide confirmation that the attenuation characteristics shown in all the complex dispersion diagrams presented carry over to a corresponding 10-unit cell long finite chain. We observe that the transmittance through a finite chain significantly reduces in a manner that directly correlates with the attenuation in the dispersion, with the two coupled attenuation peaks matching in their appearance. Noticeably, we observe that in absence of the attached resonator, the effective mass of the system becomes frequency independent.

3.7. Future extensions to more complex coupled IA-local resonance configurations

The mass-spring-inertial amplifier configuration presented in Fig. 1 is a canonical configuration that serves the purpose of providing a demonstration of the core concept of coupling an IA antiresonance with an attenuation peak associated with a standard separately attached local resonator. This cononical framework has enabled rigorous analytical characterization and investigation of the concept. However, it is readily extendable to more complex configurations in higher dimensions. For example, a quasi-1D configuration comprising multiple interconnected layers of masses and springs could form the base chain [36]. Realization using standard mechanical components such as rods and beams is also possible [22,28]. Extension to higher dimensions may be explored by considering, for example, a cage-type 2D [37] or 3D [38] structure to form the base medium from which levered substructures and separately attached local resonators could emerge. Incorporation of damping in the system—to yield metadamping behavior [39–42]—and/or nonlinearity [43–45] are also other promising future avenues of investigation.

4. Conclusions

A configurational concept for the realization of an inertial amplification band gap with double attenuation peaks has been presented. The concept is based on coupling a mass that is inertially amplified by a lever arm with a secondary mass that is separately attached to the backbone chain. This secondary mass on its own represent a conventional local resonator that may be introduced to any system as a separate attachment. Upon tuning, the antiresonance peak associated with this mass couples with that associated with the inertially amplified mass leading to a low and wide IA band gap with a characteristic double peak in the

attenuation profile. Compared to a corresponding IA chain with only a single attenuation peak and a semi-infinite but weak attenuation profile at frequencies above this peak, here we get a spatial attenuation profile that is finite in its frequency range, but strong in its intensity. A key advantage is that the band-gap edge frequencies, width, and minimum attenuation strength may all be optimized through this coupled IA-local resonance configurational concept.

Given these favorable characteristics, we derived mathematical expressions for the conditions for transition to the double-peak coupled regime. Extensive mappings of the response were then provided to conceptualize the effects of key parameters in the chain, namely the inertial amplification factor, the resonator natural frequency ratio, and the local resonator mass ratio, on the band-gap location, size, and attenuation profile. Furthermore, a vertical spring supporting the inertial amplifier mass pair is introduced to quantify—from a practical perspective–the effect of the lever link stiffness (which in our model is treated as rigid) on the degree of inertial amplification as realized in the dynamical response. Finally, three IA band-gap metrics have been introduced to characterize the band-gap relative size and attenuation properties, and a parametric optimization study was conducted to elucidate the effects of the various chain parameters on these metrics. It is observed that complex relations unfold with changing the IA and local resonator masses; for example, the minimum attenuation strength experiences an optimal point that coincides with the lowest relative band-gap size. While the proposed concept is demonstrated on a simple ID mass-spring model, it is readily extendable to more complex configurations in higher dimensions, for example by augmenting 3D IA configurations with separately attached resonating pillars [46]. These results pave the way for the design of a new class of inertially amplified phononic materials with superior IA band-gap performance characteristics.

Data availability statement

The raw/processed data required to reproduce these findings cannot be shared at this time due to technical or time limitations.

Declaration of Competing Interest

The authors declare that they have no known competing financial interests or personal relationships that could have appeared to influence the work reported in this paper.

Acknowledgment

AB acknowledges the Inspire faculty grant, grant number DST/INSPIRE/04/2018/000052, for supporting the research.

References

[1] Mead DJ. Wave propagation in continuous periodic structures: research contributions from Southampton, 1964–1995. J Sound Vib 1996;190(3):495–524.
[2] Hussein MI, Leamy MJ, Ruzzene M. Dynamics of phononic materials and structures: historical origins, recent progress, and future outlook. Appl Mech Rev 2014;66(4):40802.
[3] Banerjee A, Das R, Calius EP. Waves in structured mediums or metamaterials: areview. Arch Comput Methods Eng 2019;26(4):1029–58.
[4] Sigalas MM, Economou EN. Elastic and acoustic wave band structure. J Sound Vib 1992;158(2):377–82.
[5] Kushwaha MS, Halevi P, Dobrzynski L, Djafari-Rouhani B. Acoustic band structure of periodic elastic composites. Phys Rev Lett 1993;71(13):2022–5.
[6] Liu Z, Zhang X, Mao Y, Zhu YY, Yang Z, Chan CT, et al. Locally resonant sonic materials. Science 2000;289(5485):1734–6.
[7] Jin Y, Pennec Y, Bonello B, Honarvar H, Dobrzynski L, Djafari-Rouhani B, et al. Physics of surface vibrational resonances: pillared phononic crystals, metamaterials, and metasurfaces. Rep Prog Phys 2021. doi:10.1088/1361-6633/abdab8.
[8] Sigmund O, Søndergaard Jensen J. Systematic design of phononic band–gap materials and structures by topology optimization. Philos Trans R Soc Lond Ser A 2003;361(1806):1001–19.
[9] Bilal OR, Hussein MI. Ultrawide phononic band gap for combined in-plane and out-of-plane waves. Phys Rev E 2011;84(6):065701.
[10] Lu Y, Yang Y, Guest JK, Srivastava A. 3-D phononic crystals with ultra-wide band gaps. Sci Rep 2017;7(1):1–14.
[11] Jiang S, Hu H, Laude V. Ultra-wide band gap in two-dimensional phononic crystal with combined convex and concave holes. Phys Status Solidi-Rapid Res Lett 2018;12(2):1700317.
[12] DAlessandro L, Ardito R, Braghin F, Corigliano A. Low frequency 3D ultra-wide vibration attenuation via elastic metamaterial. Sci Rep 2019;9(1):1–8.
[13] Bilal OR, Hussein MI. Trampoline metamaterial: local resonance enhancement by springboards. Appl Phys Lett 2013;103(11):111901.
[14] Coffy E, Lavergne T, Addouche M, Euphrasie S, Vairac P, Khelif A. Ultra-wide acoustic band gaps in pillar-based phononic crystal strips. J Appl Phys 2015;118(21):214902.
[15] Banerjee A, Das R, Calius EP. Frequency graded 1D metamaterials: a study on the attenuation bands. J Appl Phys 2017;122(7):075101.
[16] Liu L, Hussein MI. Wave motion in periodic flexural beams and characterization of the transition between Bragg scattering and local resonance. J Appl Mech 2012;79(1):11003–17.
[17] Jia Z, Chen Y, Yang H, Wang L. Designing phononic crystals with wide and robust band gaps. Phys Rev Appl 2018;9(4):044021.
[18] Liu Z, Chan CT, Sheng P. Three-component elastic wave band-gap material. Phys Rev B 2002;65(16):165116.
[19] Yilmaz C, Hulbert GM, Kikuchi N. Phononic band gaps induced by inertial amplification in periodic media. Phys Rev B 2007;76(5):54309.
[20] Yilmaz C, Hulbert GM. Theory of phononic gaps induced by inertial amplification in finite structures. Phys Lett A 2010;374(34):3576–84.
[21] Acar G, Yilmaz C. Experimental and numerical evidence for the existence of wide and deep phononic gaps induced by inertial amplification in two-dimensional solid structures. J Sound Vib 2013;332(24):6389–404.
[22] Frandsen NMM, Bilal OR, Jensen JS, Hussein MI. Inertial amplification of continuous structures: large band gaps from small masses. J Appl Phys 2016;119(12):124902.
[23] Yilmaz C, Hulbert GM. Chapter 11: dynamics of locally resonant and inertially amplified lattice materials. In: Phani AS, Hussein MI, editors. Dynamics of lattice materials. John Wiley & Sons Ltd; 2017. p. 233–58.
[24] Huang H, Sun C, Huang G. On the negative effective mass density in acoustic metamaterials. Int J Eng Sci 2009;47(4):610–17.
[25] Kulkarni PP, Manimala JM. Longitudinal elastic wave propagation characteristics of inertant acoustic metamaterials. J Appl Phys 2016;119(24):245101.
[26] Al Ba'ba'a H, DePauw D, Singh T, Nouh M. Dispersion transitions and pole-zero characteristics of finite inertially amplified acoustic metamaterials. J Appl Phys 2018;123(10):105106.
[27] Taniker S, Yilmaz C. Generating ultra wide vibration stop bands by a novel inertial amplification mechanism topology with flexure hinges. Int J Solids Struct 2017;106:129–38.
[28] Li J, Li S. Generating ultra wide low-frequency gap for transverse wave isolation via inertial amplification effects. Phys Lett A 2018;382(5):241–7.
[29] Orta AH, Yilmaz C. Inertial amplification induced phononic band gaps generated by a compliant axial to rotary motion conversion mechanism. J Sound Vib 2019;439:329–43.
[30] Foehr A, Bilal OR, Huber SD, Daraio C. Spiral-based phononic plates: from wave beaming to topological insulators. Phys Rev Lett 2018;120(20):205501.
[31] Yuksel O, Yilmaz C. Realization of an ultrawide stop band in a 2-D elastic metamaterial with topologically optimized inertial amplification mechanisms. Int J Solids Struct 2020;203:138–50.
[32] Milton GW, Willis JR. On modifications of Newton's second law and linear continuum elastodynamics. Proc R Soc A 2007;463(2079):855–80.
[33] Li J, Chan CT. Double-negative acoustic metamaterial. Phys Rev E 2004;70(5):055602.
[34] Huang HH, Sun CT. Anomalous wave propagation in a one- dimensional acoustic metamaterial having simultaneously negative mass density and Youngs modulus. J Acoust Soc Am 2012;132:2887.
[35] Zhou X, Liu X, Hu G. Elastic metamaterials with local resonances: an overview. Theor Appl Mech Lett 2012;2(4):041001.
[36] Li Y, Wang X, Yan G. Configuration effect and bandgap mechanism of quasi-one-dimensional periodic lattice structure. Int J Mech Sci 2021;190:106017.
[37] Jin Y, Shi Y, Yu G-C, Wei G-T, Hu B, Wu L-Z. A multifunctional honeycomb metastructure for vibration suppression. Int J Mech Sci 2020;188:105964.
[38] Jiang W, Yin M, Liao Q, Xie L, Yin G. Three-dimensional single-phase elastic metamaterial for low-frequency and broadband vibration mitigation. Int J Mech Sci 2021;190:106023.
[39] Hussein MI, Frazier MJ. Metadamping: an emergent phenomenon in dissipative metamaterials. J Sound Vib 2013;332(20):4767–74.
[40] Bacquet CL, Hussein MI. Dissipation engineering in metamaterials by localized structural dynamics (2018) arXiv:1809.04509[physics.app–ph].
[41] Bacquet CL, Al Babaa H, Frazier MJ, Nouh M, Hussein MI. Chapter two - metadamping: dissipation emergence in elastic metamaterials. In: Hussein MI, editor. Advances in applied mechanics, 51; 2018. p. 115–64.
[42] Aladwani A, Nouh M. Mechanics of metadamping in flexural dissipative metamaterials: analysis and design in frequency and time domains. Int J Mech Sci 2020;173:105459.
[43] S LB, Jensen JS. Low-frequency band gaps in chains with attached non-linear oscillators. Int J Nonlinear Mech 2007;42:1186–93.
[44] Khajehtourian R, I HM. Dispersion characteristics of a nonlinear elastic metamaterial. AIP Adv 2014;4:124308.
[45] Xu X, Barnhart MV, Fang X, Wen J, Chen Y, Huang G. A nonlinear dissipative elastic metamaterial for broadband wave mitigation. Int J Mech Sci 2019;164:105159.
[46] Taniker S, Yilmaz C. Design, analysis and experimental investigation of three-dimensional structure with inertial amplification induced vibration stop bands. Int J Solids Struct 2015;72:88–97.